Electronic structure of rare-earth semiconducting ErN thin films determined with synchrotron radiation photoemission spectroscopy and first-principles analysis

Krithika Upadhya [1,2,5,*] Rajendra Kumar [1,2,*] Madhusmita Baral [3,4,*] Shilpa Tripathi [6]
S. N. Jha [6] Tapas Ganguli [3,4] and Bivas Saha [1,2,5,†]

[1]*Chemistry and Physics of Materials Unit, Jawaharlal Nehru Centre for Advanced Scientific Research, Bangalore 560064, India*
[2]*International Centre for Materials Science, Jawaharlal Nehru Centre for Advanced Scientific Research, Bangalore 560064, India*
[3]*Raja Ramanna Centre for Advanced Technology, Indore 452013, India*
[4]*Homi Bhabha National Institute, Training School Complex, Anushakti Nagar, Mumbai 400094, India*
[5]*School of Advanced Materials (SAMat), Jawaharlal Nehru Centre for Advanced Scientific Research, Bangalore 560064, India*
[6]*Beamline Development and Application Section, Bhabha Atomic Research Centre, Mumbai 400085, India*

Erbium nitride (ErN) is an emerging rocksalt rare-earth semiconducting pnictide and has attracted significant interest in recent years for its potential applications in thermoelectric energy conversion, spintronic devices, and for the Gifford-McMahon cryocoolers. Due to the Er intra-$4f$ electronic transition, Er-doped III-nitride semiconductors such as GaN, InGaN, etc. exhibit strong emission in the retina-safe and fiber optical communication wavelength window of $1.54\,\mu$m that is researched extensively for developing solid-state lasers, amplifiers, and light-emitting devices. However, due to ErN's propensity for oxidation in ambient, high-quality ErN thin film growth has been challenging and an in-depth understanding of its electronic structure remains unanswered. In this work, the valence band electronic structure of ErN thin films is measured with normal as well as with resonant synchrotron-radiation photoemission spectroscopy. Photoemission measurements show a valence band maximum and Fermi energy difference of $\sim$2.3 eV in ErN. First-principles density functional theory (DFT) calculations are performed not only to explain the valence band electronic structure but also to determine transport properties such as effective mass and deformation potentials. Strong localized Er-$4f$ states are observed $\sim$6–8 eV below the valence band maxima and the valence band edge is found to exhibit N-$2p$ character. Resonant photoemission data corroborates the DFT calculations. To accurately capture the electronic structure in modeling, beyond generalized gradient approximation (GGA) methods such as (a) Heyd-Scuseria-Ernzerhof hybrid functional and (b) GGA+U Hubbard correction schemes are utilized. Determination of the electronic structure of ErN marks significant progress in developing ErN-based electronic, optoelectronic, and thermoelectric devices.

I. INTRODUCTION

Erbium nitride (ErN) is an emerging semiconducting rare-earth pnictide that crystallizes in the rocksalt structure and exhibits distinctive electronic and magnetic properties [1–4]. Due to the localized strongly correlated $4f$ electrons, ErN exhibits a ferromagnetic ground state and has attracted significant interest in recent years as a potential candidate for spintronic device applications as well as to construct spin superlattices [5]. Er-doped group III-nitride semiconductors such as GaN, InGaN, etc. have been utilized for a long time to develop solid-state lasers [6,7], electroluminescent devices [8,9], amplifiers [10], and light-emitting diodes [11] as they exhibit a strong emission in the retina-safe and fiber optical communication wavelength window of $1.54\,\mu$m due to the Er intra-$4f$ electronic transitions. Such device structures have

been currently replicated for Er-doped group-IV and II-VI semiconductors such as in Si [12], ZnO [13] as well as for yttrium aluminum garnet (YAG) crystals to broaden their application space [7]. The $4f$-intra-subshell transitions in Er hold enormous promise to develop emerging and next generations of quantum light emitters as well as for single-photon emission and detection studies [14]. Micron-sized large particles of ErN exhibit a large specific heat at cryogenic temperatures (4 K) and are utilized in Gifford-McMahon cryocoolers for industrial applications [15]. Recently, Er-doped ScN has also been explored with the view of developing the field-controlled spectrally active optics [16]. In summary, ErN holds enormous potential for a broad range of electronic, optical, and magneto-optic device applications.

However, despite the interest from various fields, research and development in ErN have not progressed as much as with other transition metal or rare-earth nitride semiconductors such as ScN, GdN, etc. [17]. One of the main reasons behind the relative lack of interest in ErN is its propensity towards oxygen that makes it unstable in ambient conditions and restricts device implementation. Though research in ErN could

---

*These authors contributed equally to this work.

†Corresponding author should be addressed: bsaha@jncasr.ac.in; bivas.mat@gmail.com

be traced back to the 1960s when dense specimens and fine powders of ErN were synthesized and their optical absorption was measured [1], until now only a handful of experimental reports exist on the growth and analysis of its physical properties. Bulk ErN crystals have been synthesized in recent years on W foils with physical vapor transport method at high temperatures (1620 °C–1770 °C) inside a nitrogen pure environment [4]. Structural characterization revealed that such ErN crystals grow with (100) orientations and were highly faceted with (100) and (111) planes. Raman spectroscopy measurements revealed LO and TO, phonon at the L point and Γ point of the Brillouin zone with frequencies of 574 and 330 cm^{-1}, respectively on ErN crystals that deviated from stoichiometry with an erbium-to-nitrogen atomic ratio that ranged from 1:1.15 to 1:1.2 [4]. Theoretical calculations also showed ErN to be a tough material with a toughness to fracture ratio of 0.61 and anisotropic thermal conductivity [18].

In terms of its electronic structure, though the initial room-temperature photoluminescence (PL) measurement on bulk ErN crystal suggested a minimum direct bandgap of ∼1 eV, subsequent low-temperature PL measurement revealed the minimum bandgap to be 2.4 eV [19]. Further analysis of the PL measurement also showed two valence bands and two conduction bands at the Γ-point of the Brillouin zone separated by 0.15 and 0.34 eV, respectively [20]. Optical absorption studies on evaporated ErN film in the 1960s had shown a bandgap of 2.4 eV on sub-stoichiometric films that is consistent with the recent PL measurements [1,19]. In terms of the theoretical investigation of its electronic structure and magnetic properties, early density functional theory (DFT) calculations with local spin density approximation (LSDA) showed ErN to exhibit a nearly zero bandgap with the valence band maxima (VBM) situated at the Γ point, while the conduction band minima (CBM) located at the X point [2,21]. Since LSDA calculation is known to underestimate the bandgap of semiconductors, such observations are not surprising. However, subsequent quasiparticle self-energy correction revealed a small gap of ∼0.2 eV for ErN in its paramagnetic phase, while LSDA calculations with Hubbard-U correction (with U applied on Er-*4f* orbitals) resulted in a direct gap at the Γ point of 0.97 eV and indirect Γ-*X* gap between 0.53 and 0.65 eV depending on the magnetic transition [21]. Therefore, a considerable debate exists on the nature of ErN's electronic structure both from an experimental point of view as well as from the theoretical calculations. Since the accurate determination of the electronic structure of semiconductors is crucial for the determination and exploration of their device implementation, significant efforts are required not only to unambitiously measure the band structure of ErN but also to explain such results with theoretical underpinning.

Recently, textured ErN thin films with (002) and (111) orientations have been sputter-deposited on the (001) MgO and (0001) Al$_2$O$_3$ substrates in an ultrahigh vacuum chamber, and capped with a thin AlN layer to avoid oxidation of the film in ambient conditions. From the high-resolution x-ray diffraction pattern analysis, a *c*-plane lattice constant of 4.87 and 4.86 Å was obtained for the ErN film on MgO and Al$_2$O$_3$, respectively [22], that agrees well with the lattice parameter of bulk ErN crystals [4]. Room-temperature optical absorp-

tion measurement showed a direct transition at ∼1.9 eV and Hall measurement suggested a degenerate semiconducting electronic nature with 4.3×10^{20} to 1.4×10^{21} cm^{-3} electron concentration that presumably arises due to the presence of defects including the oxygen impurity and nitrogen vacancies [22]. The temperature-dependent thermoelectric measurement revealed that ErN thin film exhibit a moderate Seebeck coefficient of -72 μV/K at 640 K, and an appreciably high thermoelectric power factor of 0.44×10^{-3} W/mK^2 at 486 K [22]. Though the Seebeck coefficient and the power factor in ErN are smaller than its sister thermoelectric materials such as ScN [23], CrN [24], etc., an expected low thermal conductivity could give rise to high overall thermoelectric figure-of-merit (ZT) in ErN in the mid-to-high temperature range. Therefore, to determine the suitability of ErN for specific device applications, it is important to understand the electronic structure of ErN in detail. With this motivation, photoemission (PES) measurements have been carried out on sputter-deposited high-quality ErN thin films. Further, the electronic structure of ErN is modeled with beyond generalized gradient approximation (GGA) methods such as Hubbard-U corrections for the strong on-site Coulomb interaction of localized electrons with variable U parameters, as well as with Heyd-Scuseria-Ernzerhof (HSE) hybrid functional methods.

II. SAMPLE FABRICATION AND CHARACTERIZATION

ErN thin films with ∼400 nm thickness were deposited on (0001) Al$_2$O$_3$ and (001) Si substrates inside an ultrahigh vacuum chamber with a base pressure of 2×10^{-9} Torr at 760 °C. Depositions are performed at the constant power mode and an Ar: N$_2$ gas mixture ratio of 9:2 sccm is used. The chamber pressure was maintained at 10 mTorr during all the depositions. Details on the growth process are further presented in the Supplemental Material (SM) [25]. To prevent oxidation of the film in ambient conditions, a 20-nm-thick insulating AlN layer was deposited *in situ* on the ErN film at the same deposition conditions. The capping layer thickness was a bit larger keeping in mind that between the sample deposition and the synchrotron PES measurement, the sample would be exposed to ambient for about five-to-seven days. However, since the lab-source x-ray photoelectron spectroscopy (XPS) experimental station did not contain any Ar ion sputter etching facility, only a 2-nm-thick AlN was deposited on ErN film for the XPS measurement, and the sample was transferred from the growth chamber to the load lock chamber of XPS experimental station within 2 min. Core level binding energy positions and the chemical states of Er and N elements are investigated through XPS study using a nonmonochromatic Al-K$_\alpha$ lab-source (1.486 keV). The synchrotron-radiation-based PES measurements were performed at BL-3 of Indus-1 synchrotron source, RRCAT, India [26]. To identify the origin of the valence band features, resonant photoemission spectroscopy (RPES) measurements have been carried out. DFT calculations were performed with the Quantum Espresso (PWSCF) implementation code. Details about the sample growth, XPS, synchrotron PES, and the DFT calculations are presented in the SM [25].
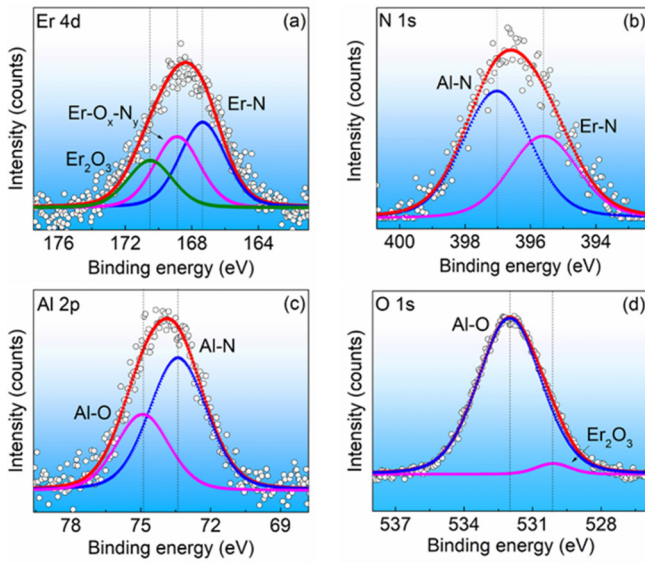
FIG. 1. XPS core-level spectra of ErN film corresponding to (a) Er-4d (b) N-1s (c) Al-2p and (d) O-1s peaks are presented. As the ErN film was capped with 2 nm AlN, XPS signal arise from both the AlN and ErN layers.

III. RESULTS AND DISCUSSIONS

A. X-ray photoelectron spectroscopy (XPS)

To understand the core-level electronic states and chemical shifts, first, the XPS data were analyzed. Since the top AlN layer thickness was kept very small (2 nm), the survey scan shows signals from both the AlN and ErN layers with a very small contribution from carbon and oxygen surface contamination. The binding energy position of the core-level peaks such as Al-2p, Er-4d, N-1s, and O-1s was calibrated using the reference C-1s photoelectron signal at 284.6 eV. The XPS core-level spectra of these elements were deconvoluted into subpeaks using the Voigt function, which were then assigned to the particular chemical state as shown in Fig. 1. In the Er-4d core-level peak, there are three deconvoluted subpeaks at 167.4, 168.9, and 170.5 eV binding energies [see Fig. 1(a)], which are assigned to Er-N, Er-O$_x$-N$_y$, and Er$_2$O$_3$, respectively. Since the binding energy position of the Er-4d peak in metallic Er is reported to be around 167.25 eV [27,28] and there is no literature available for the Er-4d peak position corresponding to the ErN, we have assigned the deconvoluted subpeak at 167.4 eV to be the Er-4d state in Er-N bond. The peak centered at 168.9 eV corresponds to the oxynitride contribution from the film which was also previously observed in the XPS core-level spectra of Ti-2p in TiN thin film [29]. However, a sufficient number of XPS studies have been carried out on Er$_2$O$_3$ that matches well with the lower intensity Er$_2$O$_3$ peak obtained in this study and hence confirms its binding energy position at 170.5 eV [30]. In the case of the N-1s peak, the deconvoluted subpeaks are centered at 395.6 eV and 397 eV [see Fig. 1(b)]. One of the peaks located at 395.6 eV is assigned to Er-N and the other subpeak at 397 eV is attributed to the presence of N in the Al-N bond, which agrees well with the previous studies on AlN [31–33]. Similarly, the chemical bonding in the film
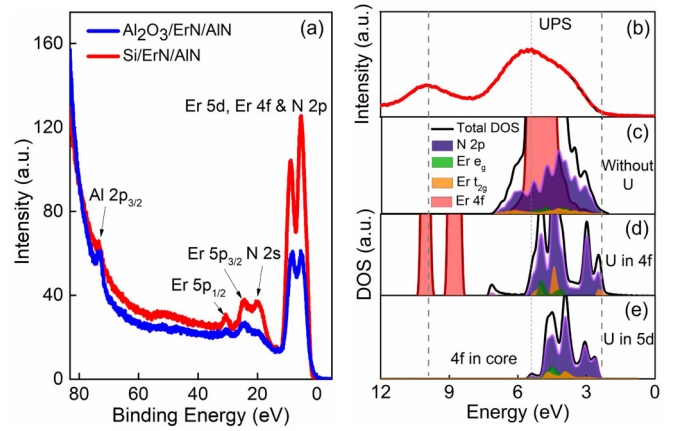

FIG. 2. (a) Synchrotron-radiation photoemission spectra of ErN thin-films after significantly sputtering out the top 20 nm AlN capping layer that shows its valence band electronic states. (b) The valence band shows the Er-4f and Er-5d, N-2p hybridized states well as the valence band edge. (c) The total and partial DOS of the N-2p, Er-4f and Er-5d states was calculated using GGA and without U correction (d) The total and partial DOS of the N-2p Er-5d and Er-4f states was calculated using GGA+U with U = 7 eV for Er-4f states where Er-4f electrons are considered as valence electrons. The valence band edge and Er-4f states align well with the experimental photoemission spectra. (e) The total and partial DOS of the N-2p and Er-5d states was calculated using GGA+U with U = 6 eV for Er-5d states where Er-4f electrons are treated as core.

was further analyzed using the XPS data of the Al-2p [see Fig. 1(c)] with appropriate curve-fitting lines, whose result indicates the presence of Al-N bond at 73.4 eV [34] and Al-O bond at 74.9 eV [35,36]. The observation of the Al-O bond is most apparently due to the tendency of the AlN capping layer to undergo surface oxidation [36,37]. The core-level scan of O-1s [see Fig. 1(d)] has been deconvoluted into two subpeaks. The very low-intensity peak at 530.1 eV reveals the existence of a trace amount of O present as Er$_2$O$_3$ in the film [38]. The presence of Er$_2$O$_3$, despite the AlN protective layer, is due to the persistent target contamination that is caused by the high affinity of Er towards oxygen, which probably has led to its incorporation during the growth process itself. Whereas, the high-intensity subpeak situated at 531.9 eV is attributed to the presence of oxygen in the form of Al$_2$O$_3$ that is formed due to the oxidation of the top AlN capping layer [36,39].

B. Synchrotron photoemission spectroscopy (PES) and resonant PES (RPES) spectra

For a detailed understanding of the valence band electronic structure, the synchrotron PES data have been recorded and analyzed. Due to the presence of the top AlN layer, the as-deposited films exhibit a peak at ∼73.4 eV, corresponding to the Al-2$p_{3/2}$ states in AlN [34] (see Fig. S1 in the SM [25]). As the top AlN layer is sputtered away, the Al-2$p_{3/2}$ peak intensity decreases progressively and the ErN signal appears in the photoemission spectra. A total sputtering time of ∼2 hours at 1 keV was required to remove the 20-nm-thick AlN top layer with the help of a defocused Ar$^+$ ion gun. As shown in Fig. 2(a), the synchrotron PES spectra of ErN

film deposited on Al_2O_3 and Si substrates exhibit very similar spectral features. A small peak observed at ∼30.7 eV in the PES spectrum belongs to the Er-$5p_{1/2}$ state, which is consistent with the literature reports [40]. The peaks centered at ∼24.8 and 20 eV correspond to the Er-$5p_{3/2}$ and N-2s states, which is consistent with the literature reports of metallic Er and 2s states of N bonded with transition metals [41,42]. Since there is no literature available to date for the photoemission spectrum of ErN, the comparison of the binding energy position of Er-$5p_{3/2}$ peak could only be made with Er metal. In the PES spectrum [shown in Fig. 2(a)], the valence band is found to be spread in the energy range from Fermi level (E_F) to 12.5 eV, with two well-separated peaks. We refer to these features as A in the energy range of 2.4 to 8 eV and B in the range of 8 to 12 eV. These valence band peaks are primarily dominated by the Er-4f and hybridized Er-5d, and N-2p state, with a small contribution from O-2p states that originates from the presence of residual oxygen in the film because of the target contamination [43]. This assignment of the Er and N associated features is based on the available literature of valence band density of states reported for Er_2O_3 [44]. These aspects are addressed through resonant PES data analysis and first-principles calculations in the following discussion.

Further, the valence band region recorded at 41 eV is shown in Fig. 2(b) for the ErN film on Si, where the binding energy separation between the VBM (E_{VBM}) and the E_F is found to be ∼2.3 eV. Though the position of ErN's Fermi energy is determined by the electronic properties such as carrier concentration, effective mass, etc., Since the present ErN contains a large carrier concentration in the 4.3×10^{20}–1.4×10^{21} cm^{-3} range [22], thus E_F is expected to reside close to or inside the conduction band. Therefore, the measured energy separation ($E_{VBM} - E_F$) should be close to its bandgap. It is interesting to note that the measured $E_{VBM} - E_F$ in this work is slightly higher than the bandgap measured with absorption spectroscopy studies on similar films [22]. However, it is closer to the bandgap determined with the PL measurement on bulk ErN [20] as well as to the old absorption study in the 1960s [1]. Though the exact origin of this difference is currently unknown, *n*-type defects such as oxygen impurities and nitrogen vacancies in ErN are expected to populate states close to the conduction band edges and may reduce the absorption edge with Urbach tailing. Such subbandgap absorption could have resulted in a smaller bandgap compared to the $E_{VBM} - E_F$ measured with PES studies.

For better understanding of the nature of states near to the VBM, RPES spectra of ErN/Si thin film is measured at various photon energies and is shown in Fig. 3. Two distinct and well-separated peaks are found at binding energies of ∼5.5 eV and ∼9 eV in the valence band, which are marked as A and B, respectively. As the photon energy varies from 31 to 176 eV, there is a significant change of intensities of the A and B features in the valence band. At lower photon energy, feature B has a relatively lower intensity compared to feature A. As the photon energy approaches the Er 4d-4f resonance at ∼167 eV, the intensity of feature A decreases, whereas the intensity of feature B increases significantly. This observation indicates that feature B at a higher binding energy of ∼9 eV (∼6.6 eV below the E_{VBM}) primarily corresponds to Er-4f states. The photoemission spectra of Er metal and
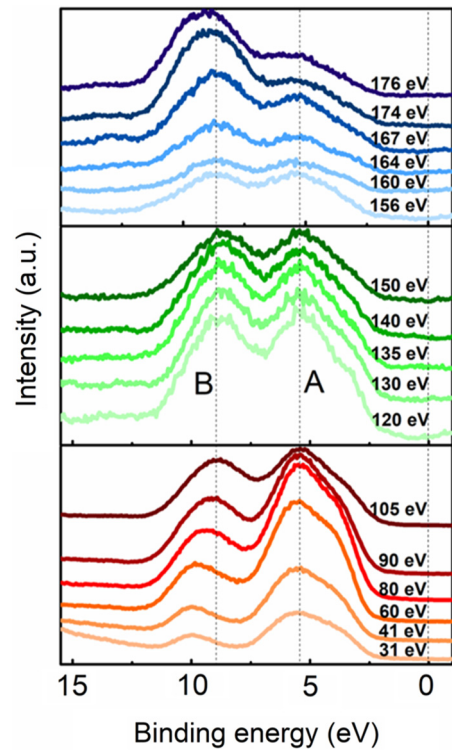

FIG. 3. Resonant photoemission spectra of ErN thin film deposited on the Si substrate at various photon energy is presented. Well-separated and distinct two peaks at ∼5.5 eV (A) and ∼9 eV (B) are observed in the valence band.

Er_2O_3 show that the position of Er-4f states are ∼5 to 8.5 eV below the VBM [30,41,45–47] which is within the range of our experimentally observed Er-4f states in ErN. To further confirm the distribution of partial density of valence band states, a preliminary analysis of the valence band data for different excitation energies is carried out by plotting the constant initial state spectra and presented in the SM [25].

In addition, to gain further insight into the valence band electronic structure, the valence band spectrum measured at 41 eV is compared with the density of states (DOS) calculated without and with Hubbard-U corrections for both Er-5d and Er-4f states separately as it was not possible to apply U corrections for both d and f states simultaneously in Quantum Espresso code [shown in Figs. 2(c), 2(d), and 2(e)]. Here, the calculated valence band edge is aligned with the experimental valence band edge of ErN. Figure 2(c) shows that the Er-4f states are found just below the E_{VBM} (∼2–4 eV) and overlap with Er-5d and N-2p states in the absence of any U correction. However, experimental PES spectra show the presence of Er-4f states far below the E_{VBM} (∼6.6 eV). It is well known that traditional DFT does not capture the strong correlation in the d and f orbitals. Thus, to capture the accurate position of Er-4f states, we have applied U correction of 7 eV for Er-4f states [see Fig. 2(d)]. Note that, U values of 7–10 eV for rare-earth nitrides have been used in the literature [21]. The Er-4f states are found to be highly localized inside the valence band and exhibit a doublet with the peak positions at 6.4 and 7.6 eV below the E_{VBM}, respectively. In the experimental spectrum, however, they appear as one peak, because

of instrumental broadening, possible effects of the presence of a small amount of oxygen, and other final state effects. As the RPES measurements with various photon energy suggest that the $4f$ electrons are localized in nature and their states are found deep inside the valence band, we have considered them as core electrons and applied U correction for Er-$5d$ states for further calculations to obtain accurate valence band edge and the bandgap [Fig. 2(e)]. Therefore, note that for all the calculations in this work [except for Fig. 2(c) and 2(d)] the Er-$4f$ electrons are treated as core and the U parameter is applied for Er-$5d$ states. Only for the calculation of PDOS in Figs. 2(c) and 2(d), Er-$4f$ electrons are treated as valence electrons and the U parameter is applied for only Er-$4f$ state in Fig. 2(d). The U value of 6 eV for Er-$5d$ states [Fig. 2(e)] results in a bandgap close to the experimentally observed bandgap which is discussed in detail subsequently. From the calculated partial DOS (PDOS) shown in Fig. 2(e), the valence band is found to be spread from ∼2.3 to 5.5 eV and is dominated by the hybridized Er-$5d$ and N-$2p$ states, which is consistent with other transition metal pnictides such as ScN, ZrN, HfN, etc. [42,43,48,49]. The calculated PDOS of N-$2p$ matches quite well with the experimental PES with a broadening towards higher energy due to the presence of small oxygen impurity in the ErN consistent with the PES of another well-known rare-earth pnictide ScN [43].

C. Electronic structure calculations

Band structure calculations performed using GGA exchange-correlation functional results in an indirect bandgap of 0.2 eV along the Γ-X direction [see Fig. 4(c)] that is consistent with the previous reports [21]. The GGA approach in DFT is well-known to significantly underestimate the bandgap of the semiconductors. Thus, the HSE and GGA+U methods are adopted to obtain the correct bandgap in ErN. The fraction of the exact exchange (α) in the hybrid functional calculation is varied from 0.15 to 0.25 [see Fig. 4(a)], which resulted in an upward shifting of the conduction band states, while the valence band remains relatively unchanged. For $\alpha = 0.20$, an indirect bandgap of ∼2.4 eV is obtained that is close to the experimentally observed bandgap in this study (assuming a very small shift in the E_F due to the Moss-Burstein effect) as well as that reported in one of the other previous study [20]. The total DOS for $\alpha = 0.20$ is shown in Fig. 4(b).

The GGA+U calculation [see Fig. 4(c)] performed with a Hubbard-U correction of 6 eV for the Er-$5d$ states where Er-$4f$ electrons are treated as core, show that the CBM dominated by Er-$5d$ states [see Figs. 3(d) and 4] become more localized. Such localization of the Er-$5d$ states leads to an increase of the Γ-X bandgap and a decrease in the Γ-Γ bandgap of ErN. For U = 6 eV, an indirect bandgap of 2.15 eV from Γ to X and a direct bandgap of 2.55 eV at Γ point is obtained. Calculation with U = 7 eV changes the nature of the electronic structure with the indirect gap becoming larger than the direct bandgap (see Table I). It is interesting to note that in one of the earlier reports an indirect bandgap of 0.20 eV was reported for ErN along the Γ-X direction, where the U parameter was used for Er-$4f$ orbitals instead of the $5d$ states [21]. If the U parameter is used for $4f$ states it will
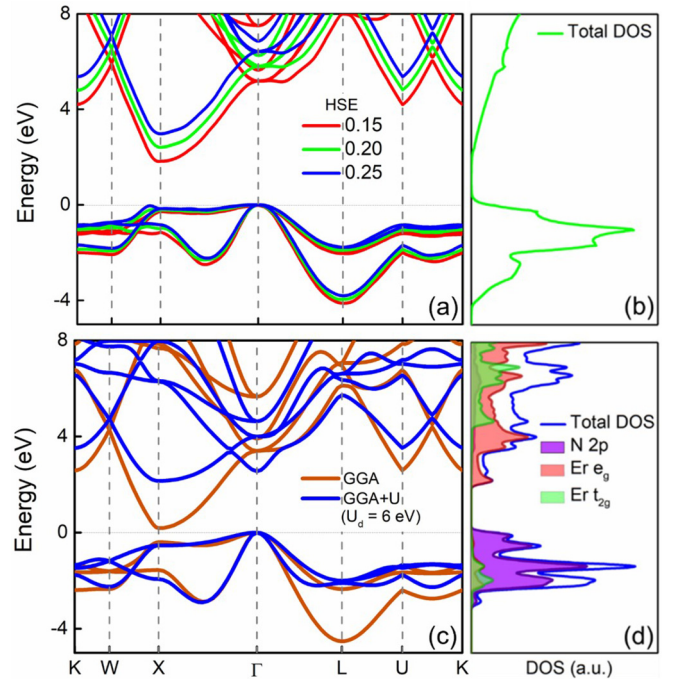

FIG. 4. (a) Electronic band structure of ErN calculated using HSE functional with various exact exchange (α) values. Bandgap increases with an increase in the α values. (b) Corresponding total DOS for $\alpha = 0.20$. (c) Band structure of ErN calculated using GGA and GGA+U with a U parameter of 6 eV for the Er-$5d$ states where Er-$4f$ electrons are treated as core electrons. (d) Corresponding total and partial DOS for U = 6 eV in Er-$5d$ states.

only localize the $4f$ states whereas, the CBM of ErN mainly consists of the Er-$5d$ states. Previously, for the determination of the bandgap in GdN, a sister rare-earth nitride of ErN and where both the Gd-$4f$ and $5d$ states are present, the Hubbard U correction is used for the Gd-$5d$ states with U = 8 eV instead of $4f$ states to explain the experimentally observed bandgap [50]. Thus, it is necessary to apply U correction for the Er-$5d$ orbitals to obtain the correct bandgap in ErN. The total DOS and partial density of N-$2p$ and Er-$5d$ states are plotted for U = 6 eV in Fig. 4(d).

TABLE I. Calculated direct and indirect bandgap of ErN at different regions of the dispersion spectrum determined with GGA+U method with various U parameters and HSE method with various α values. m_l^* and m_t^* are the longitudinal and transverse effective masses calculated at CBM (X point for U = 0−6 eV and Γ point for U = 7 eV).

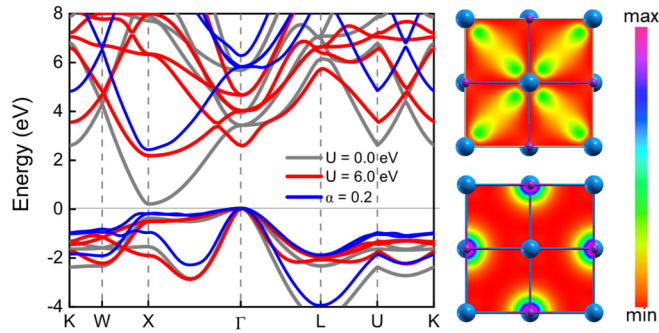| U (eV)	$E_g^{\Gamma\text{-}X}$ (eV)	$E_g^{\Gamma\text{-}\Gamma}$ (eV)	$E_g^{X\text{-}X}$ (eV)	m_l^* (m_0)	m_t^* (m_0)
0	0.18	3.41	0.58	1.24	0.11
2	0.88	3.31	1.34	1.61	0.21
4	1.39	3.00	1.89	2.03	0.30
6	2.15	2.55	2.69	3.34	0.41
7	2.69	2.23	3.25	0.18	0.18
$\alpha = 0.20$	2.41	5.81	2.62	0.739	0.213
$\alpha = 0.25$	2.97	6.42	3.13	0.666	0.297

FIG. 5. Comparison of the ErN band structure calculated using GGA, GGA+U (with U = 6 eV for Er-5d states), and HSE functional (with $\alpha = 0.2$). Both the GGA+U and HSE, shift the Er-5d states to higher energy and open higher bandgap. The charge densities are shown on the right-hand side correspond to CBM + 100 meV (top) and VBM - 100 meV (bottom) for the GGA+U method with U = 0 eV. Blue and violet spheres correspond to Er and N, respectively. Charge densities look similar for the other two methods as well.

The band structure of ErN calculated using various mechanisms such as GGA, GGA+U (U = 6 eV for Er-5d states with Er-4f electrons as core), and HSE ($\alpha = 0.20$) are plotted together for comparison (see in Fig. 5). All three mechanisms show similar valence band structures but significantly different conduction band structures. The introduction of the U parameter results in flattening of Er-5d states, however, HSE functional shifts the conduction band states without affecting the curvature of the bands. The charge density plots at the CBM and VBM are shown in Fig. 5, which reveals that CBM is mainly populated with the Er-5d states, whereas the VBM consists of N-2p states.

For evaluation of the transport properties, the electron effective masses at the CBM (X point for U = 0−6 eV) along both the longitudinal (X-W) and transverse directions (X-Γ) have been calculated by fitting the quadratic function to the corresponding band energies. For U = 7 eV, the effective mass is calculated at Γ point along the Γ-X and Γ-K directions. At the X point, with an increase in the U parameter (U = 0−6 eV), a monotonic increase in the effective masses can be observed due to the localization of the Er-5d orbitals. The effective mass estimated here is comparable to other rare-earth nitrides [51–53]. Note that, since the effective mass for U = 7 eV is calculated at Γ point (CBM) instead of X point, it is not found to be following the increasing trend like the one at X point. Whereas, the effective mass calculated using the HSE method also gives comparable values with the GGA+U method but does not show any trend with increasing α values.

The volume deformation potentials (α_ν) are further calculated using the formula $dE_g^\alpha/d\ln(V/V_0)$ for bandgaps $E_g^{\Gamma\text{-X}}$, $E_g^{\Gamma\text{-}\Gamma}$, and $E_g^{\text{X-X}}$ and are presented in Table II. Here, V_0 is

TABLE II. Estimated deformation potential for the bandgaps $E_g^{\Gamma\text{-X}}$, $E_g^{\Gamma\text{-}\Gamma}$ and $E_g^{\text{X-X}}$ using GGA, GGA+U, and HSE functional.

U (eV)	$\alpha_\nu^{\Gamma-X}$	$\alpha_\nu^{\Gamma-\Gamma}$	α_ν^{X-X}
0	2.04	−1.40	2.89
2	2.30	−8.95	3.05
4	2.90	−9.10	3.58
6	3.69	−8.93	4.30
7	4.13	−8.72	4.67
$\alpha = 0.2$ (HSE)	1.54	−2.08	2.36
$\alpha = 0.25$ (HSE)	1.39	−2.31	2.20

the volume of the fully relaxed system and V is the volume of the strained system. Estimated values (see Table II) of deformation potential are comparable to other rare-earth nitrides reported in the literature [51].

IV. CONCLUSION

In conclusion, conventional as well as resonant synchrotron-radiation photoemission spectroscopy measurements are performed on highly-crystalline ErN thin films to determine the valence band electronic structure. Valence band maxima and the Fermi energy exhibits an energy difference of ∼2.3 eV that is close to the bandgap of ErN obtained in previous bulk samples. From DFT calculations, the valence band maxima and the conduction band minima are found to be dominated by the N-2p and Er-5d states, respectively. Localized Er-4f orbitals are found inside the valence band spanning an energy range of ∼6–8 eV below E_{VBM}. XPS measurements are utilized to gain insight into the core level states. DFT modelling with GGA along with a Hubbard-U correction captures the excited states and results in close to the experimental bandgap. The HSE hybrid functional is also utilized for bandgap modeling. Determination of the electronic structure of ErN with photoemission measurements and its theoretical verification mark significant progress in ErN research and will help to develop ErN based electronic, magnetic, and optoelectronic devices with improved efficiencies.

The data that supports the findings of this study are available from the corresponding author upon reasonable request.

[1] N. Sclar, Properties of rare earth nitrides, J. Appl. Phys. **35**, 1534 (1964).

[2] F. Natali, B. J. Ruck, N. O. V. Plank, H. J. Trodahl, S. Granville, C. Meyer, and W. R. L. Lambrecht,

Rare-earth mononitrides, Prog. Mater. Sci. **58**, 1316 (2013).

[3] C. Meyer, B. J. Ruck, A. R. H. Preston, S. Granville, G. V. M. Williams, and H. J. Trodahl, Magnetic properties of ErN Films, J. Magn. Magn. Mater. **322**, 1973 (2010).

[4] H. A. Al Atabi, Z. F. Al Auda, B. Padavala, M. Craig, K. Hohn, and J. H. Edgar, Sublimation growth and characterization of erbium nitride crystals, Cryst. Growth Des. **18**, 3762 (2018).

[5] A. G. Petukhov, W. R. L. Lambrecht, and B. Segall, Electronic structure of rare-earth pnictides, Phys. Rev. B **53**, 4324 (1996).

[6] Z. Y. Sun, J. Li, W. P. Zhao, J. Y. Lin, and H. X. Jiang, Toward the realization of erbium-doped GaN Bulk crystals as a gain medium for high energy lasers, Appl. Phys. Lett. **109**, 052101 (2016).

[7] N. Ter-Gabrielyan, V. Fromzel, X. Mu, H. Meissner, and M. Dubinskii, Resonantly pumped single-mode channel waveguide Er:YAG laser with nearly quantum defect limited Efficiency, Opt. Lett. **38**, 2431 (2013).

[8] J. Palm, F. Gan, B. Zheng, J. Michel, and L. C. Kimerling, Electroluminescence of erbium-doped silicon, Phys. Rev. B **54**, 17603 (1996).

[9] A. J. Steckl, J. C. Heikenfeld, Dong-Seon Lee, M. J. Garter, C. C. Baker, Yongqiang Wang, and R. Jones, Rare-earth-doped GaN: Growth, properties, and fabrication of electroluminescent devices, IEEE J. Sel. Top. Quantum Electron. **8**, 749 (2002).

[10] R. Dahal, C. Ugolini, J. Y. Lin, H. X. Jiang, and J. M. Zavada, Erbium-doped GaN optical amplifiers operating at 1.54 μm, Appl. Phys. Lett. **95**, 111109 (2009).

[11] R. Dahal, C. Ugolini, J. Y. Lin, H. X. Jiang, and J. M. Zavada, 1.54 Mm emitters based on erbium doped InGaN p-i-n junctions, Appl. Phys. Lett. **97**, 141109 (2010).

[12] T. Dejima, R. Saito, S. Yugo, H. Isshiki, and T. Kimura, Effects of hydrogen plasma treatment on the 1.54 μm luminescence of erbium-doped porous silicon, J. Appl. Phys. **84**, 1036 (1998).

[13] S. Bhatia, N. Verma, and R. K. Bedi, Optical application of er-doped ZnO nanoparticles for photodegradation of direct red - 31 dye, Opt. Mater. (Amst). **62**, 392 (2016).

[14] A. Alizadehkhaledi, A. L. Frencken, F. C. J. M. van Veggel, and R. Gordon, Isolating nanocrystals with an individual erbium emitter: a route to a stable single-photon source at 1550 nm wavelength, Nano Lett. **20**, 1018 (2020).

[15] T. Nakano, S. Masuyama, Y. Hirayama, T. Izawa, T. Nakagawa, Y. Fujimoto, T. Irie, E. Nakamura, and T. A. Yamamoto, ErN and HoN spherical regenerator materials for 4 K cryocoolers, Appl. Phys. Lett. **101**, 251908 (2012).

[16] H. Kim, Y. Park, G. C. King, K. Lee, and S. H. Choi, Effect of doping with rare earth elements (Er, Ho) on smart optical materials (ScN, AlN) in an applied electric field, in *SPIE Smart Structure/NDE 2012*, edited by V. K. Varadan, (2012), Vol. 8344, p. 8344-31.

[17] F. Natali, N. O. V. Plank, J. Galipaud, B. J. Ruck, H. J. Trodahl, F. Semond, S. Sorieul, and L. Hirsch, Epitaxial growth of GdN on silicon substrate using an AlN buffer layer, J. Cryst. Growth **312**, 3583 (2010).

[18] V. Bhalla and D. Singh, Anisotropic assessment of ultrasonic wave velocity and thermal conductivity in ErX (X:N, As), Indian J. Pure Appl. Phys. **54**, 40 (2016).

[19] M. A. McKay, Q. W. Wang, H. A. Al-Atabi, Y. Q. Yan, J. Li, J. H. Edgar, J. Y. Lin, and H. X. Jiang, Band structure and infrared optical transitions in ErN, Appl. Phys. Lett. **116**, 171104 (2020).

[20] M. A. McKay, H. A. Al-Atabi, J. Li, J. H. Edgar, J. Y. Lin, and H. X. Jiang, Band structure and ultraviolet optical transitions in ErN, Appl. Phys. Lett. **118**, 131108 (2021).

[21] P. Larson, W. R. L. Lambrecht, A. Chantis, and M. van Schilfgaarde, Electronic structure of rare-earth nitrides using the LSDA+U approach: importance of allowing 4f orbitals to break the cubic crystal symmetry, Phys. Rev. B **75**, 045114 (2007).

[22] K. Upadhya, V. Bhatia, A. I. Kamalasanan Pillai, M. Garbrecht, and B. Saha, High thermoelectric power factor in ambient-stable semiconducting rare-earth ErN thin films, Appl. Phys. Lett. **118**, 132103 (2021).

[23] D. Rao, B. Biswas, E. Flores, A. Chatterjee, M. Garbrecht, Y. R. Koh, V. Bhatia, A. I. K. Pillai, P. E. Hopkins, M. Martin-Gonzalez, and B. Saha, High mobility and high thermoelectric power factor in epitaxial ScN thin films deposited with plasma-assisted molecular beam epitaxy, Appl. Phys. Lett. **116**, 152103 (2020).

[24] P. Eklund, S. Kerdsongpanya, and B. Alling, Transition-metal-nitride-based thin films as novel energy harvesting materials, J. Mater. Chem. C **4**, 3905 (2016).

[25] See Supplemental Materials at http://link.aps.org/supplemental/10.1103/PhysRevB.105.075138 for details about sample growth, XPS, synchrotron PES, and the DFT calculations (n.d.).

[26] N. C. Das, S. N. Jha, S. V. N. Bhaskara Rao, B. N. Rajasekhar, S. S. Bhattacharya, S. K. Sikka, A. V. Korgaonkar Jagannath, K. G. Bhushan, J. V. Yakhmi, and V. C. Sahani, Development of angle resolved photoelectron spectroscopy beamline at indus-1 synchrotron radiation source, J. Opt. **32**, 27 (2003).

[27] C. J. Powell, Recommended auger parameters for 42 elemental solids, J. Electron Spectros. Relat. Phenomena **185**, 1 (2012).

[28] C. J. Powell, Elemental binding energies for X-Ray photoelectron spectroscopy, Appl. Surf. Sci. **89**, 141 (1995).

[29] S. Nayak, S. Acharya, M. Baral, M. Garbrecht, T. Ganguli, S. M. Shivaprasad, and B. Saha, Schottky barrier height of epitaxial lattice-matched TiN/Al 0.72 Sc 0.28 N metal/semiconductor superlattice interfaces for thermionic energy conversion, Appl. Phys. Lett. **115**, 251901 (2019).

[30] N. Guerfi, O. Bourbia, and S. Achour, Study of erbium oxidation by XPS and UPS, Mater. Sci. Forum **480–481**, 193 (2005).

[31] R. Dalmau, R. Collazo, S. Mita, and Z. Sitar, X-Ray photoelectron spectroscopy characterization of aluminum nitride surface oxides: thermal and hydrothermal evolution, J. Electron. Mater. **36**, 414 (2007).

[32] H. Oikawa, R. Akiyama, K. Kanazawa, S. Kuroda, I. Harayama, K. Nagashima, D. Sekiba, Y. Ashizawa, A. Tsukamoto, K. Nakagawa, and N. Ota, Deposition and characterization of amorphous aluminum nitride thin films for a gate insulator, Thin Solid Films **574**, 110 (2015).

[33] J. A. Perez Taborda, H. R. Landazuri, and L. P. V. Londono, Correlation between optical, morphological, and compositional properties of aluminum nitride thin films by pulsed laser deposition, IEEE Sens. J. **16**, 359 (2016).

[34] M. Alevli, C. Ozgit, I. Donmez, and N. Biyikli, Structural properties of AlN films deposited by plasma-enhanced atomic

layer deposition at different growth temperatures, Phys. Status Solidi **209**, 266 (2012).

[35] M. Alizadeh, H. Mehdipour, V. Ganesh, A. N. Ameera, B. T. Goh, A. Shuhaimi, and S. A. Rahman, Plasma-assisted hot filament chemical vapor deposition of AlN thin films on ZnO buffer layer: toward highly c-axis-oriented, uniform, insulative films, Appl. Phys. A **117**, 2217 (2014).

[36] P. Motamedi and K. Cadien, XPS analysis of AlN thin films deposited by plasma enhanced atomic layer deposition, Appl. Surf. Sci. **315**, 104 (2014).

[37] V. Rontu, P. Sippola, M. Broas, G. Ross, T. Sajavaara, H. Lipsanen, M. Paulasto-Kröckel, and S. Franssila, Atomic layer deposition of AlN from $AlCl_3$ using NH_3 and Ar/NH_3 plasma, J. Vac. Sci. Technol. A **36**, 021508 (2018).

[38] F.-H. Chen, J.-L. Her, Y.-H. Shao, Y. H. Matsuda, and T.-M. Pan, Structural and electrical characteristics of high-κ Er_2O_3 and Er_2TiO_5 gate dielectrics for a-IGZO thin-film transistors, Nanoscale Res. Lett. **8**, 18 (2013).

[39] S. W. King, J. P. Barnak, M. D. Bremser, K. M. Tracy, C. Ronning, R. F. Davis, and R. J. Nemanich, Cleaning of AlN and GaN surfaces, J. Appl. Phys. **84**, 5248 (1998).

[40] M. Pugaczowa-Michalska, A. Kowałczyk, G. Chełkowska, and T. Toliński, XPS spectra and electronic structure of the $ErNi_4B$ Compound, J. Alloys Compd. **385**, 44 (2004).

[41] B. D. Padalia, W. C. Lang, P. R. Norris, L. M. Watson, and D. J. Fabian, X-ray photoelectron core-level studies of the heavy rare-earth metals and their oxides, Proc. R. Soc. London Ser. A. **354**, 269 (1977).

[42] S. Badrinarayanan, S. Sinha, and A. B. Mandale, XPS Studies of nitrogen ion implanted zirconium and titanium, J. Electron Spectros. Relat. Phenomena **49**, 303 (1989).

[43] S. Nayak, M. Baral, M. Gupta, J. Singh, M. Garbrecht, T. Ganguli, S. M. Shivaprasad, and B. Saha, Rigid-band electronic structure of scandium nitride across the n -type to p -type carrier transition regime, Phys. Rev. B **99**, 161117 (2019).

[44] J. Costa-Quintana and F. Lopez-Aguilar, Metal-semiconductor transition in the electronic structure of 4f materials: Application to Er_2O_3, J. Phys. C **15**, 6741 (1982).

[45] P. O. Hedén, H. Löfgren, and S. B. M Hagström, 4f Electronic States in the Metals Nd, Sm, Dy, and Er Studied by X-Ray Photoemission, Phys. Rev. Lett. **26**, 432 (1971).

[46] G. Brodén, UV-photoemission measurements on erbium and samarium, Phys. Kondens. Mater. **15**, 171 (1972).

[47] Ultra-violet photoemission of erbium exposed to oxygen, water and hydrogen | Semantic Scholar, https://www.semanticscholar.org/paper/Ultra-violet-photoemission-of-erbium-exposed-to-and-Netzer-Wille/a1a639dc57659d14c26a86d45b1ebac65cbe4af0.

[48] D. Gall, M. Städele, K. Järrendahl, I. Petrov, P. Desjardins, R. T. Haasch, T.-Y. Lee, and J. E. Greene, Electronic structure of ScN determined using optical spectroscopy, photoemission, and *ab initio* calculations, Phys. Rev. B **63**, 125119 (2001).

[49] B. Saha, T. D. Sands, and U. V. Waghmare, Thermoelectric properties of HfN/ScN metal/semiconductor superlattices: a first-principles study, J. Phys.: Condens. Matter **24**, 415303 (2012).

[50] H. J. Trodahl, A. R. H. Preston, J. Zhong, B. J. Ruck, N. M. Strickland, C. Mitra, and W. R. L. Lambrecht, Ferromagnetic redshift of the optical Gap in GdN, Phys. Rev. B **76**, 085211 (2007).

[51] B. Saha, T. D. Sands, and U. V. Waghmare, Electronic structure, vibrational spectrum, and thermal properties of yttrium nitride: A first-principles study, J. Appl. Phys. **109**, 073720 (2011).

[52] S. Zerroug, F. Ali Sahraoui, and N. Bouarissa, *Ab initio* calculations of yttrium nitride: structural and electronic properties, Appl. Phys. A Mater. Sci. Process. **97**, 345 (2009).

[53] N. K. Allam, B. S. Shaheen, and A. M. Hafez, Layered Tantalum oxynitride nanorod array carpets for efficient photoelectrochemical conversion of solar energy: experimental and DFT Insights, ACS Appl. Mater. Interfaces **6**, 4609 (2014).